ACADEMIA ROMÂNĂ
Revue Roumaine de Chimie
https://www.icf.ro/rrch/

Rev. Roum. Chim.,
2026, *71*(5–6), 373–387
DOI: 10.33224/rrch.2026.71.5-6.08

PHOTOCATALYTIC DEGRADATION OF CARMINE DYE USING Mn-DOPED IRON OXIDE NANOSTRUCTURES

Pratibha BHARDWAJ,[a] Y. C. GOSWAMI[b,*] and U. P. S GAHLAUT[a]

[a] Nano Lab, School of Sciences, ITM University, Gwalior MP, India 474001
[b] SVIS, Shri Vaishnav Vidyapeeth Vishwavidyalaya, Indore, India 453111

Received December 19, 2026

Increasing urbanization and industrialization in the last two centuries put pressure on natural resources. This double-edged sword of industrial development has increased wastewater discharge in rivers or other natural sources of water. In this manner this contaminated water is harmful to both aquatic ecosystem and human health. All over the world different research groups have addressed this problem by applying various technologies. Out of various treatment technologies adsorption is one of the most popular because it can remove specific pollutants efficiently and selectively. Magnetic adsorbent, like hematite (α-Fe_2O_3) has emerged as an Excellent adsorbent material due to their large surface area and affinity towards various functional groups. In this research article we have prepared Manganese (Mn) doped iron oxide nanoparticles via a co-precipitation method. The size and morphology of the nanoparticles were characterized using scanning electron microscopy (SEM), and X-ray diffraction (XRD), along with UV-Vis and infrared (IR) spectroscopy. The SEM analysis revealed that the nanoparticles were rod-shaped with an average length of 127.632 nm and the XRD patterns confirmed the successful formation of Mn-doped iron oxide nanoparticles were, Rhombohedral in shape with an average crystal size of 17.1579 nm. Particles have shown excellent potential for the removal of carcinogenic dyes from wastewater.

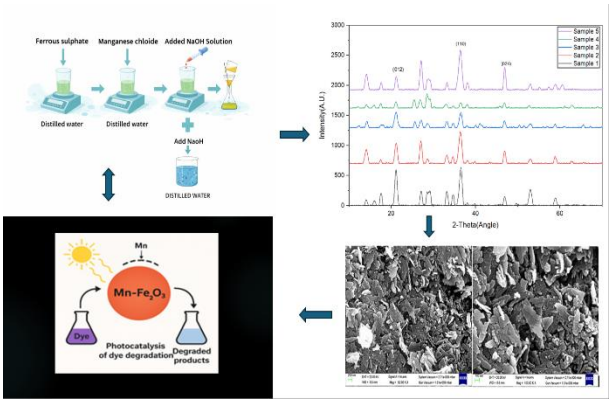

INTRODUCTION

The swift expansion among the world's population, together with the complex impacts of industrialization and economic progress over the past century, has intensified the scarcity of clean and safe water. Ensuring access to potable water is vital not only for maintaining public health but also for supporting sustainable economic growth. Unfortunately, increasing contamination from dyes, heavy metals, anions, and various hazardous pollutants has turned water pollution into a major environmental and health related challenge worldwide.[1] According to United Nations estimates,

* Corresponding author: ycgoswami@gmail.com

approximately 3.1% of global deaths equivalent to nearly 1.7 million annually are linked to inadequate access to clean water.[2] Water pollutants can broadly be classified into biodegradable and nonbiodegradable categories. Among these, non-biodegradable pollutants pose a more severe risk due to their persistence and harmful nature. Many such pollutants are carcinogenic, teratogenic, hepatotoxic, or genotoxic, thereby raising serious concerns for the survival and health of living organisms. Industrial wastewater released from industries such as textiles, paper manufacturing, mining, plastics, and pharmaceuticals often carries significant amounts of dye pollutants.[3–5] Which can adversely impact human and ecological health.[6] Even trace concentrations of dyes can alter water transparency and reduce gas solubility, thereby limiting sunlight penetration and oxygen availability for aquatic life.[7] This ecological imbalance emphasizes the critical necessity for efficient methods to treat contaminated water prior to discharge.[8–10]

Nanotechnology has recently emerged as a transformative discipline, with applications extending from diagnostics and targeted drug delivery to disease treatment and clean water technologies.[11–15] In wastewater treatment, nanotechnology offers significant potential due to the versatility and efficiency of nanomaterials.[16,17] Conventional methods for treating wastewater using methods such as membrane filtration, chemical precipitation, ion exchange, and adsorption, are commonly employed.[18,19] Among these, adsorption is considered particularly advantageous due to its cost effectiveness, recyclability, lower environmental hazard, and broad applicability.[20] Various nanomaterials, including metal-based nanoparticles, carbon-based materials, chalcogenide semiconductors, and metal oxide photocatalysts, have been investigated for wastewater treatment.[21,22] Notably, nanostructured transition metal oxides have gained significant interest because of their ability to exist in various phases, each offering distinct structural, physicochemical, and application specific properties. For instance, metal oxides such as zinc oxide (ZnO), titanium dioxide (TiO_2), and iron oxide (Fe_2O_3 /Fe_3O_4) exhibit remarkable photocatalytic performance and high adsorption capacity, attributed to their large surface areas and functional group affinities.[23] Among these, iron oxide has attracted great attention due to its natural abundance, low cost, ease of synthesis, and environmental compatibility.[24,25] Iron oxide exists in multiple polymorphs, including iron oxides including hematite (α-Fe_2O_3), magnetite (Fe_3O_4), wurtzite (FeO), and maghemite (γ-Fe_2O_3)and less common phases such as ε-Fe_2O_3 and β-Fe_2O_3.[26] Of these, α-Fe_2O_3 exhibits the highest thermodynamic stability at room temperature,[27] It has a narrow band gap (2.2 eV, corresponding to ~564 nm in the visible spectrum),[28] along with desirable properties such as chemical and photochemical stability, non-toxicity, corrosion resistance, and magnetism. These features make it appropriate for a wide range of uses, such as biomedicine, gas detection, supercapacitors, as well as especially photocatalytic degradation of organic pollutants like dyes in wastewater,[29–32] within this work, iron oxide nanoparticles doped with manganese (Mn) were produced through a co-precipitation technique. Their structural and morphological features were examined using techniques including Scanning Electron Microscopy (SEM), X-ray Diffraction (XRD), UV-Visible (UV-Vis) spectroscopy, and Infrared (IR) spectroscopy. The results verified the effective preparation of iron oxide nanoparticles doped with manganese (Mn), exhibiting a distinct rod-shaped morphology. The prepared nanoparticles demonstrated excellent potential for the adsorption and elimination of cancer-causing dyes from wastewater, underscoring their utility within sustainable water purification technologies.

EXPERIMENTAL

Reagents Used

Ferrous sulphate heptahydrate ($FeSO_4 \cdot 7H_2O$), sodium hydroxide pellets (NaOH), and manganese chloride tetrahydrate ($MnCl_2 \cdot 4H_2O$) were procured from Fisher Scientific Pvt. Ltd. (Powai, Mumbai, Maharashtra, India) and used without further purification. Vim gel was employed as a surfactant/cleaning agent, and distilled deionized water was employed during the entire experiment work.

Synthesis of Fe2O3 Iron Oxide Nanoparticles (Sample 1)

To begin the synthesis; a solution was formed by combining 5 mL of dishwashing liquid (vim gel) together with 50 mL of distilled water. From this stock solution, 5 mL was taken and diluted further with30 millilitres of purified water. Into this

mixture, 0.5 M (4.17 g) of ferrous sulphate heptahydrate ($FeSO_4 \cdot 7H_2O$, Fisher Scientific Pvt. Ltd.) was introduced, followed by continuous stirring on a magnetic stirrer for 30 minutes. Separately, 0.5 M (0.6 g) sodium hydroxide (NaOH) pellets (Fisher Scientific Pvt. Ltd.) were dissolved in 30 mL of distilled water and kept at 10 °C. This chilled NaOH solution was slowly introduced, drop by drop, into the ferrous sulphate mixture while stirring continuously. Immediate precipitation occurred, and the solid product was separated by filtration. The precipitate was thoroughly rinsed with distilled water to remove impurities and any remaining reactants.

The collected precipitate was dried at 100 °C and then calcined at 300 °C to enhance its crystallinity. After drying, the material was ground into a fine powder, yielding Mn-doped iron oxide nanoparticles.

Synthesis of Mn-Doped Iron Oxide ($FeMn_2O_4$) Nanoparticles (Sample 2-5)

To prepare the doped nanoparticles, a soap solution was first obtained prepared by combining 5 mL of dishwashing liquid with 50 mL of distilled water. From this stock,5 mL was extracted and then diluted using 30 mL of distilled water. Into this mixture, 0.5 M (4.17 g) ferrous sulphate heptahydrate ($FeSO_4 \cdot 7H_2O$, Fisher Scientific Pvt. Ltd.) was added, followed by continuous magnetic stirring for 30 minutes. Manganese chloride tetrahydrate ($MnCl_2 \cdot 4H_2O$, Fisher Scientific Pvt. Ltd.) was then introduced into the ferrous sulphate solution in different concentrations. **(**Sample 2: 0.1 M, Sample 3: 0.2 M, Sample 4: 0.3 M, and Sample 5: 1.5 M). The mixture was continuously stirred for another 30 minutes to achieve a homogeneous distribution of the dopant ions.

In a separate container, 0.5 M (0.6 g) sodium hydroxide (NaOH) pellets were dissolved in 30 mL of distilled water, and the solution was cooled to 10 °C. This chilled NaOH solution was then added slowly, drop by drop, to the $FeSO_4$, $MnCl_2$ mixture while stirring continuously. The addition of NaOH caused the immediate formation of a precipitate. The resulting precipitate was collected via filtration and thoroughly washed with distilled water to remove any unreacted reagents and residual ions. The purified material was dried at 100 °C and subsequently calcined at 300 °C to improve its crystallinity. Finally, the dried material was finely ground to obtain Mn-doped iron oxide Nano powder.

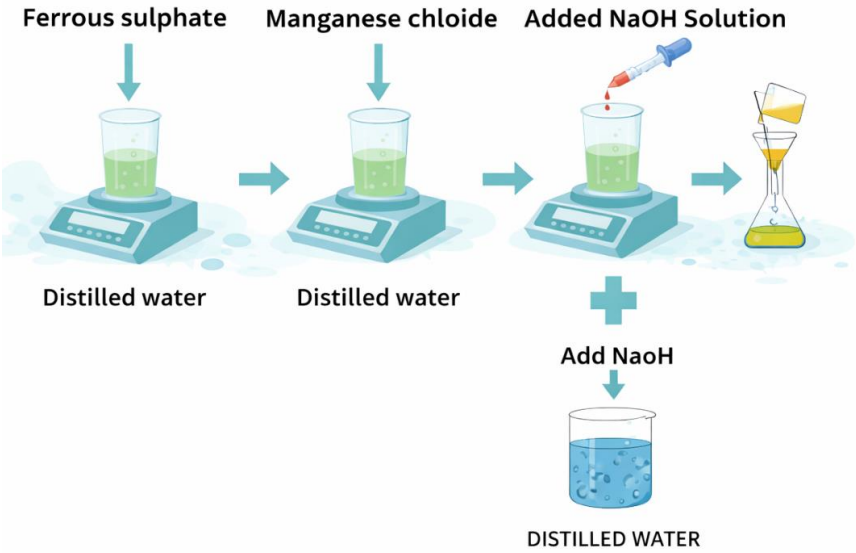

Fig.1 – Synthesis process of iron oxide/Mn- doped iron oxide nano particles.

Photocatalytic experiment

The photocatalytic degradation experiments were performed using Indigo Carmine dye as a model pollutant. A stock dye solution was prepared by dissolving 0.01 g of Indigo Carmine in 100 mL of distilled water. For each experiment, 100 mL of dye solution was taken in a quartz reaction beaker and 0.001 g of Mn-doped iron oxide nanoparticles was added as the photocatalyst.

Prior to light irradiation, the suspension was magnetically stirred in the dark for 30 minutes to

establish adsorption–desorption equilibrium between dye molecules and catalyst surface. The photocatalytic reaction was carried out under visible light irradiation using a 300 W Xenon lamp as the light source. The lamp provided radiation in the wavelength range of 400–700 nm, with an average light intensity of approximately 100 mW cm^{-2} at the reaction surface. The distance between the light source and reaction vessel was maintained at 15 cm.

During irradiation, the suspension was continuously stirred to ensure uniform dispersion of the catalyst. At regular time intervals of 10 minutes, approximately 3 mL aliquots were withdrawn and centrifuged to remove the catalyst particles. The clear supernatant was analyzed using UV–Vis spectroscopy to monitor the decrease in absorbance of Indigo Carmine at its characteristic wavelength.

All experiments were performed at room temperature (25 ± 2 °C). Control experiments were also conducted in the absence of catalyst and in the dark to confirm that dye degradation occurred only due to photocatalytic activity.

The degradation efficiency was calculated using the following relation:

Degradation (%) = $((C_0 - C_t) / C_0) \times 100$

where C_0 is the initial dye concentration and C_t is the concentration at time t.

Characterization

The synthesized Fe_2O_3 nanoparticles (Sample 1) and Mn-doped Fe_2O_3 nanoparticles (Samples 2–5) were characterized through a range of spectroscopic and microscopic techniques. The optical properties were analysed using a PerkinElmer Lambda 25 UV-Vis spectrophotometer at ITM University, Gwalior. The nanoparticle morphology was examined via scanning electron microscopy (SEM, Zeiss Aperol) at IIT Roorkee. Crystalline structures were investigated using X-ray diffraction (XRD) at Jiwaji University, Gwalior. Additionally, Fourier-transform infrared spectroscopy (FTIR, Spectrum 2, PerkinElmer) at ITM University, Gwalior, was employed to study the functional groups and bonding characteristics of the samples

RESULTS AND DISCUSSION

Structural analysis (XRD)

Powder X-ray diffraction (XRD) was employed to examine the crystalline structure of both pure Fe_2O_3 and Mn-doped Fe_2O_3 nanoparticles, with the resulting diffraction patterns presented in Figs. 2(a–f). XRD analysis was conducted to determine the phase composition and to investigate the crystalline characteristics of the synthesized samples. The diffraction patterns displayed intense and sharp peaks at 2θ values of 24° (012), 26° (012),151 35° (110), 43° (202), 49° (024), and 57.4° (122), consistent with the standard references JCPDS card No. 00-033-0664, confirming the rhombohedral in shape with an average crystal size of 17.1579nm phase of hematite (α-Fe_2O_3). The presence of these well-defined peaks suggests a high crystallinity for the synthesized nanoparticles. The Debye–Scherrer equation was employed to calculate the average crystallite size of Fe_2O_3 and Mn-doped Fe_2O_3 nanoparticles with varying Mn doping levels, as follows:

$$D = \frac{K\lambda}{\beta \cos\theta}$$

In this equation, D denotes the average crystallite size in nanometres, k is the shape factor (assumed to be 0.9), and λ represents the wavelength of the X-ray source used (Cu Kα radiation, λ = 0.15406 nm). The term $\beta_{1/2}$ corresponds to the full width at half maximum (FWHM) of the diffraction peak measured in radians, and θ is the Bragg angle related to the respective peak. The calculated crystallite sizes for Fe_2O_3 and Mn-doped Fe_2O_3 nanoparticles were found to decrease slightly with increasing Mn content, suggesting that Mn incorporation into the Fe_2O_3 lattice inhibited crystal growth and induced lattice strain.

The undoped sample is confirmed to be single-phase Fe2O3 with a rhombohedral structure.

In the case of Mn-doped samples (0.1–1.5 M), all major diffraction peaks remain consistent with Fe_2O_3, and no additional reflections corresponding to secondary phases such as $FeMn_2O_4$ were observed within the detection limit of the instrument. Furthermore, a systematic shift in peak positions was observed with increasing Mn concentration, indicating the successful incorporation of Mn ions into the Fe_2O_3 lattice rather than the formation of a separate phase The obtained Fe_2O_3 and Mn – doped Fe_2O_3 nano particle sizes were 15.50 nm, 15.93 nm, 16.23 nm, 17.15 nm and 17.35 nm respectively.

The Williamson-Hall plot was used to estimate the crystallite size and lattice strain, providing additional insight into the structural properties of the samples

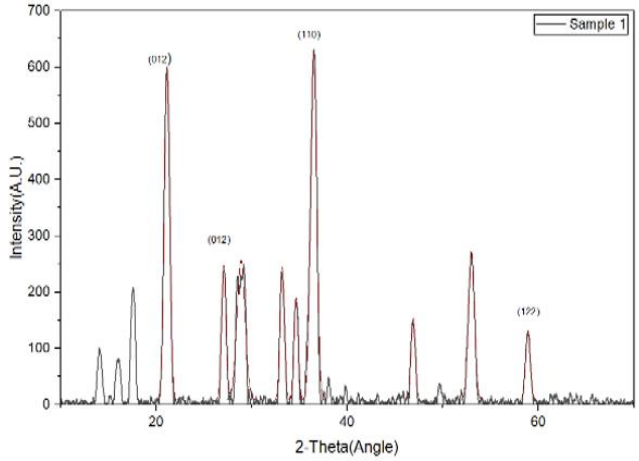

Fig(a).XRD Spectra of Sample 1 (Un-doped)

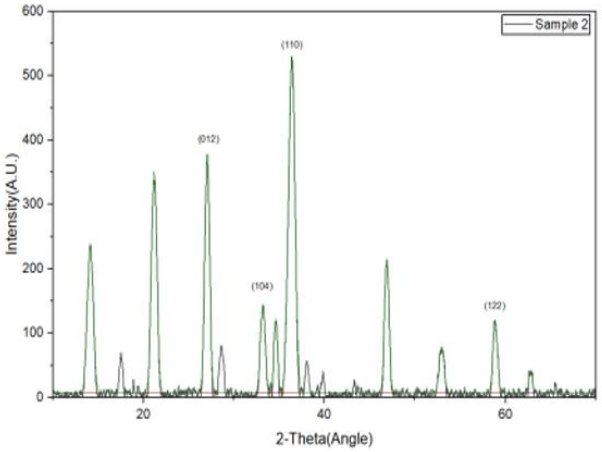

Fig(b). XRD Spectra of Sample 2

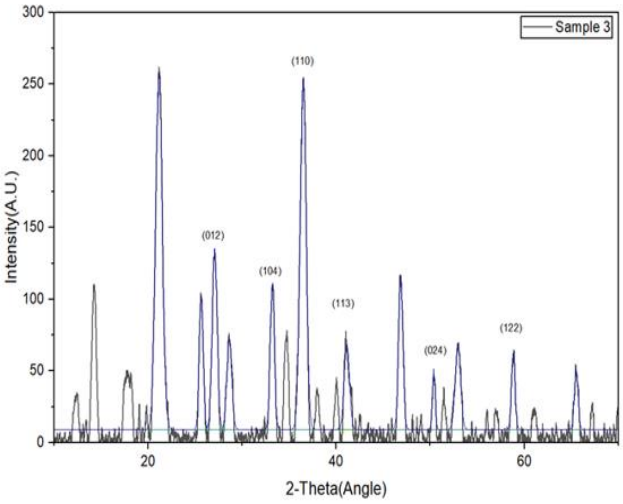

Fig(c). XRD spectra of Sample 3

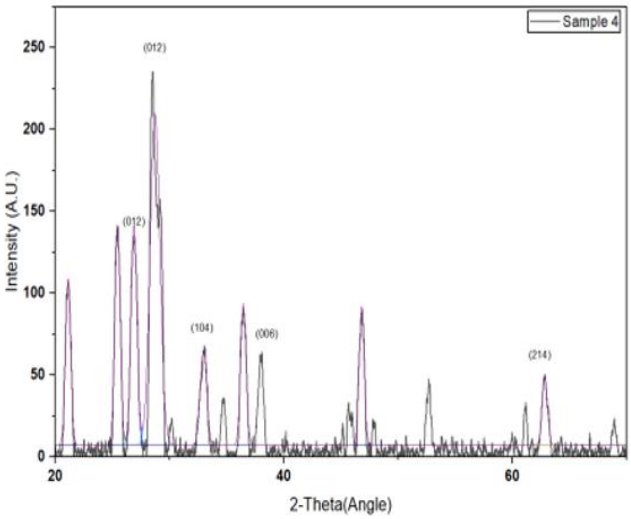

Fig(d).XRD Spectra of Sample 4

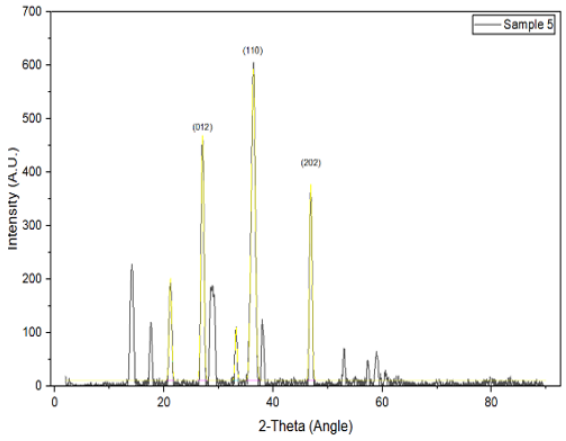

Fig (e).XRD spectra of Sample 5

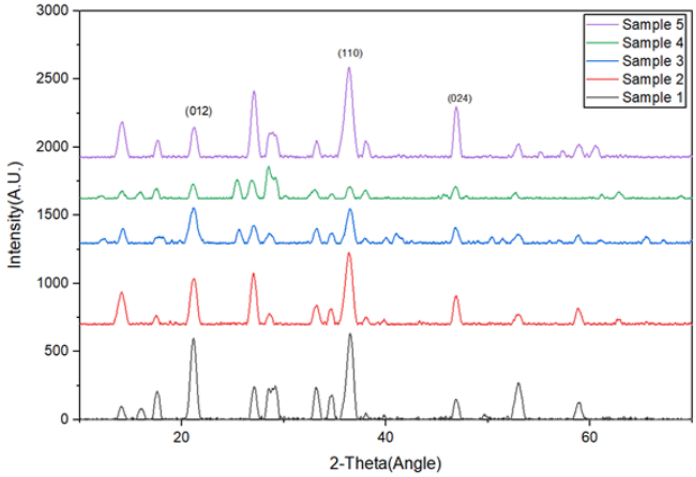

Fig (f). Combined XRD Spectra

Fig. 2 (a–f) – XRD Spectra of iron oxide /Mn-doped Iron oxide nanoparticles: a) sample 1: undoped; b) sample 2: 0.1 M; c) sample 3: 0.2 M; d) sample 4: 0.3 M; e) sample 5: 1.5 M; f) combined graph.

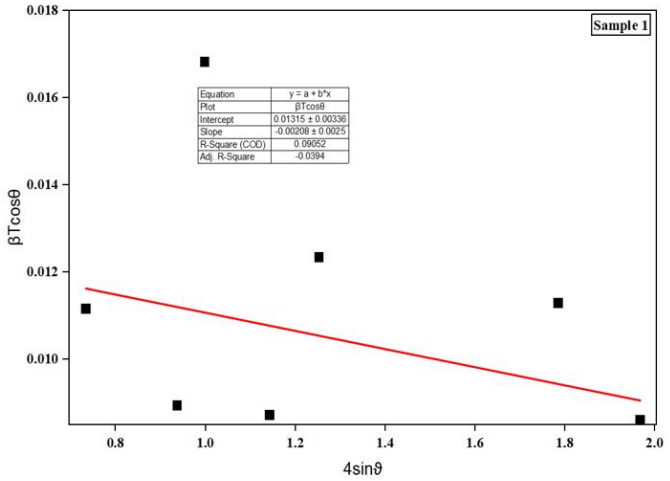

Fig(a). WH PLOT of Sample 1 (un -doped)

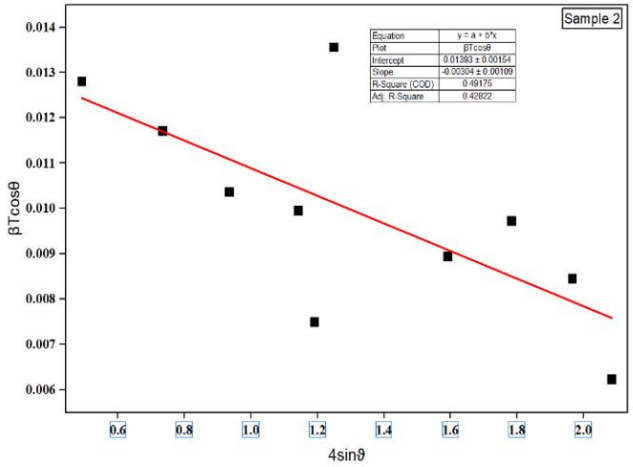

Fig (b).WH Plot of Sample 2

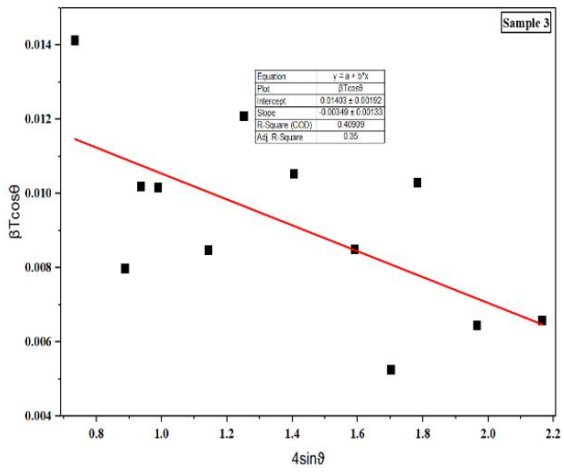

Fig (C). WH plot of Sample 3

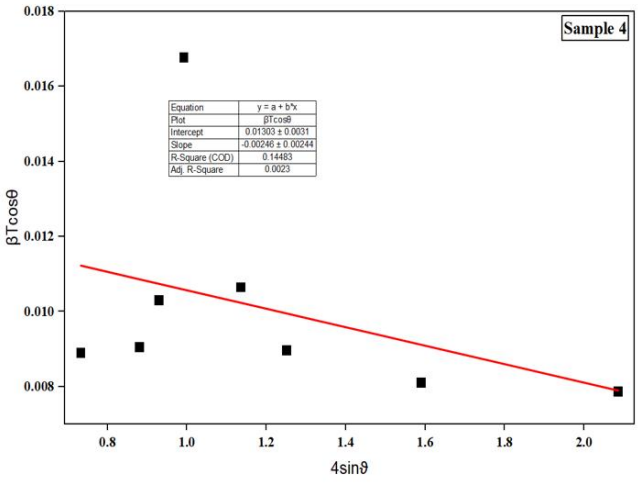

Fig (d). WH plot of Sample 4

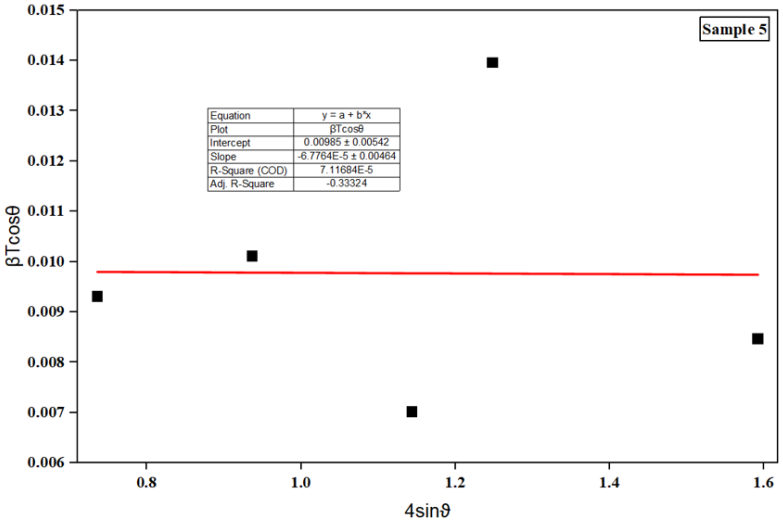

Fig(e). WH plot of Sample 5

Fig. 3(a–-e) – Williamson-Hall plot iron oxide /Mn -doped iron oxide nanoparticles: a) sample 1: undoped; b) sample 2: 0.1 M; c) sample 3: 0.2 M; d) sample 4: 0.3 M; e) sample 5: 1.5 M.

Table 1
Particle size and strain using WH plot

SAMPLE	FWHM in Radians	Size of particles D (nm)	Intercept	Strain
Sample 1	0.0126	10.55	0.01315	0.002
Sample 2	0.0128	9.96	0.01399	0.003
Sample 3	0.0143	9.89	0.01403	0.003
Sample 4	0.0090	10.64	0.01303	0.002
Sample 5	0.0104	14.08	0.00985	0.0006

Fourier Transform Infrared spectroscopy

Fourier Transform Infrared analysis spectrum belonging to undoped Fe_2O_3 nanoparticles (Sample 1), presented in Fig. 4a. shows a distinct signal observed at 3584 cm^{-1}, attributed to the stretching mode of free O–H groups. A broad and intense band at 3252 cm^{-1} is attributed to hydrogen-bonded O–H stretching, suggesting the existence of surface-adsorbed water molecules. Medium-intensity absorption bands at 1589 cm^{-1} and 1396 cm^{-1} arise from N–H bending and O–H bending vibrations, respectively. Additionally, the band at _1068__ cm^{-1} corresponds to the C–O stretching vibration

The FTIR spectrum of the Mn-doped Fe_2O_3 nanoparticles (Sample 5), shown in Fig. 4f, exhibits a sharp O–H stretching band at approximately 3589 cm^{-1}. The band at _1394__ cm^{-1} is attributed to C–O stretching vibrations. A prominent absorption band near 1068 cm^{-1} is attributed to overlapping C–O and S=O stretching modes, suggesting that Mn incorporation slightly alters the surface functional groups of Fe_2O_3.

Overall, the FTIR analysis confirms that both undoped and Mn-doped Fe_2O_3 nanoparticles possess surface hydroxyl and carbonyl-type functional groups. These groups are known to influence adsorption behaviour and contribute significantly to the photocatalytic degradation of dyes.

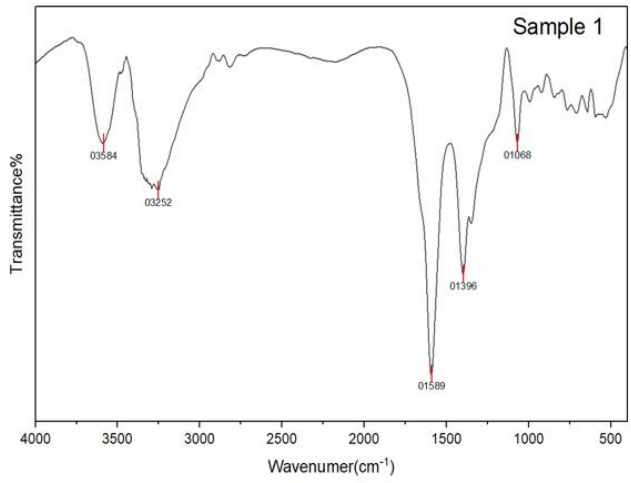

Fig(a).FTIR Spectra of Sample 1(Un-doped)

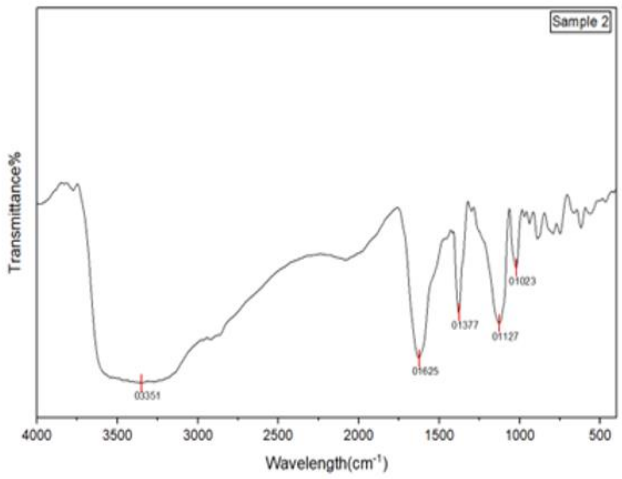

Fig(b).FTIR Spectra of Sample 2

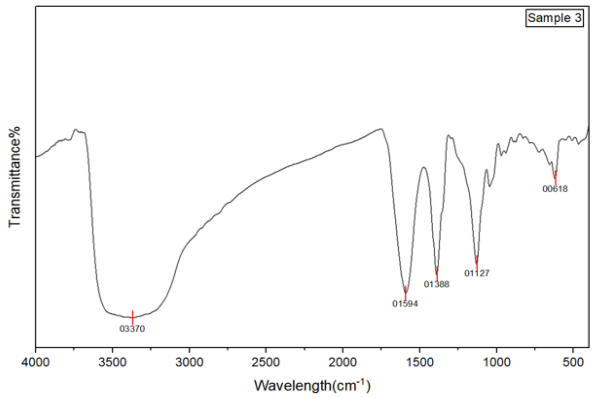

Fig(c).FTIR Spectra of Sample 3

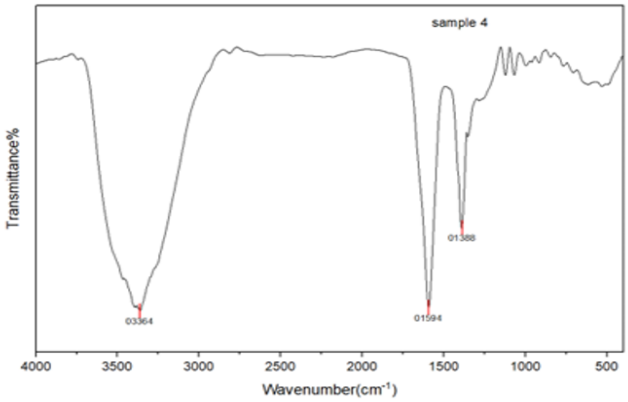

Fig(d).FTIR Spectra of Sample 4

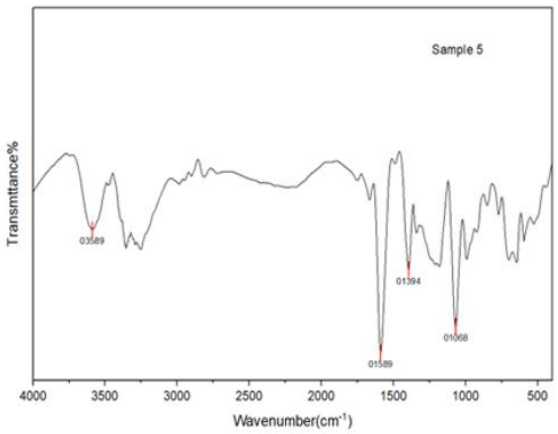

Fig(e).FTIR Spectra of Sample 5

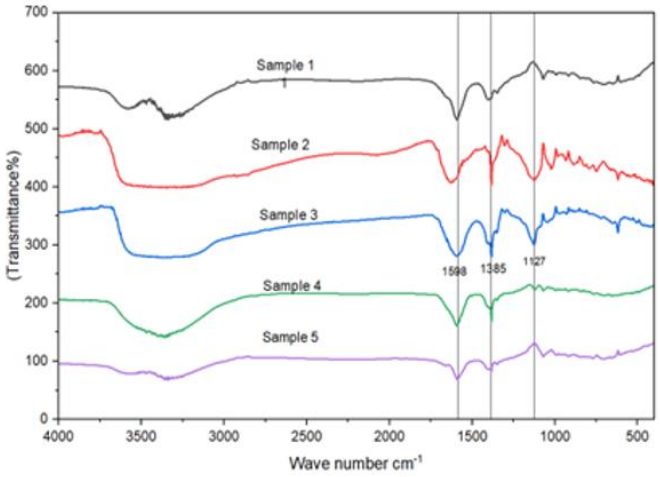

Fig(f). Combined FTIR Spectra

Fig. 4(a–f) – FTIR Spectra of iron oxide/Mn-doped iron oxide nanoparticles.

Table 2

FTIR peaks representation table

Sample (peaks) Wave no cm^{-1}	Sample 1	Sample 2	Sample 3	Sample4	Sample 5
Assignment					
O-H (stretch free vibration)	3584	-	--	-	3589
O-H (stretching vibration)	3252	3351	3370	3364	--
N-H (Bending vibration)	1589	1625	1594	1594	1589
O-H (Bending vibration)	1396	1377	1388	1388	1394
C-O (stretching vibration)	1068	1127	1127	-	1068
S=O (stretching vibration)	-	1023	0618	--	

Morphological studies (SEM)

The surface morphology was investigated using scanning electron microscopy (SEM) elemental composition, as well as mapping belonging to undoped as well as Mn-doped iron oxide nanoparticles, illustrated in Fig. 5a. The SEM micrographs of un-doped Fe_2O_3 nanoparticles exhibited mainly a rod-shaped morphology with an average length of 127.6 nm. The larger particle observed in SEM is due to agglomeration of smaller Nano crystallites. Upon doping with manganese, noticeable changes in surface morphology and particle distribution were observed. The Mn-doped nanoparticles exhibited more irregular or slightly elongated shapes, depending on the dopant concentration. In addition, the surfaces of Mn-doped particles appeared relatively rougher compared to undoped Fe_2O_3, indicating modifications in surface chemistry and crystal growth patterns due to Mn incorporation. Such morphological alterations are expected to enhance the material's photocatalytic performance through increasing the surface-active sites and improving light–matter interactions.

The histogram analysis shows that all five samples have noticeable differences in their particle size distribution, which reflects the effect of the synthesis conditions. Sample 1(un-doped) mainly consists of smaller particles in the 30–40 nm range. Sample 2 shows a wider spread of particles from 20–40 nm, indicating both small and medium-sized particles. Sample 3 has particles mostly between 40–60 nm, showing a moderate distribution. Sample 4 contains larger particles in the 70–80 nm range, suggesting higher particle growth. On the other hand, sample 5 shows a more uniform distribution around 50–60 nm, which indicates better control over particle formation. Overall, these variations in particle size can influence the surface properties and performance of the material.

The particle sizes observed in SEM appear larger than the crystallite sizes calculated from XRD. This difference arises because SEM measures the physical particle size, which may consist of agglomerated clusters of several nanocrystallites, whereas XRD provides the size of coherently diffracting crystalline domains. The crystallite sizes calculated using the Debye–Scherrer method (~15–17 nm) indicate that each rod-like particle observed in SEM is composed of multiple smaller nanocrystals. Such aggregation is typical for iron oxide nanoparticles due to magnetic interactions and high surface energy, leading to the formation of larger secondary particles.

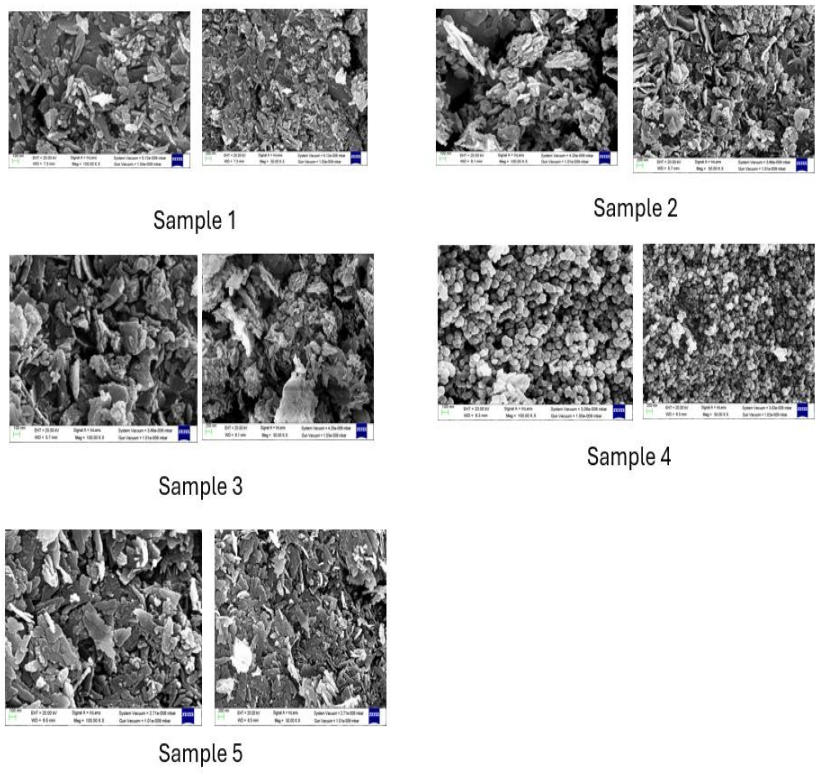

–.

Fig. 5a – Scanning electron micrograph images iron oxide /Mn -doped iron oxide nanoparticles. (sample 1: undoped sample 2: 0.1 M, sample 3: 0.2 M, sample 4: 0.3 M and sample 5: 1.5 M)

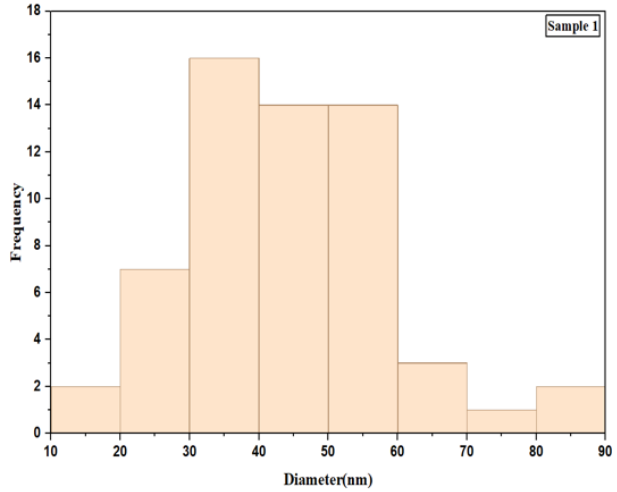

Histogram graph of Sample 1 (Un –doped)

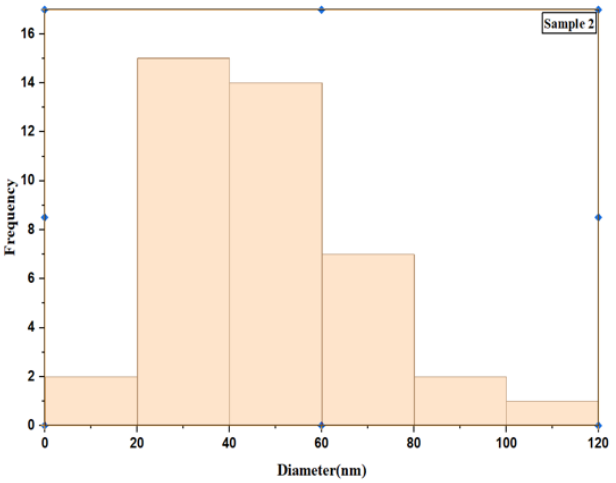

Histogram graph of Sample 2

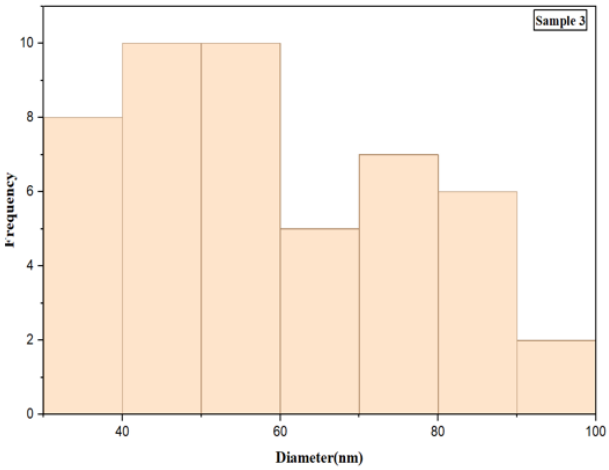

Histogram Graph of Sample 3

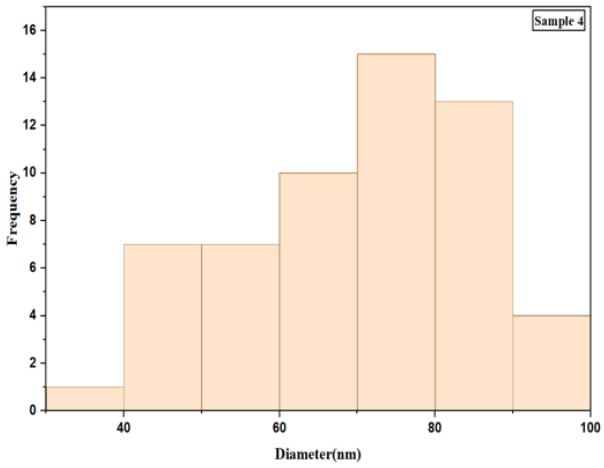

Histogram graph of Sample 4

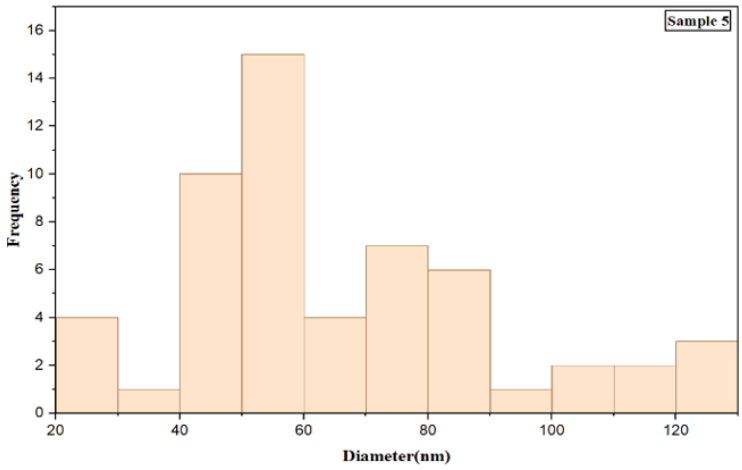

Histogram graph of Sample 5

Fig. 5b – Histogram graphs of SEM analysis iron oxide /Mn -doped Iron oxide nanoparticles: a) sample 1: undoped,; b) sample 2: 0.1 M; c) sample 3: 0.2 M; d) sample 4: 0.3 M; e) sample 5: 1.5 M.

UV-Vis Spectroscopy

The ultraviolet–visible absorption profile of Mn-doped iron oxide nanoparticles is presented in the accompanying Figure5.Incorporation of Mn caused a clear displacement of the absorption edge toward longer wavelengths, where the peak moving toward longer wavelengths. This shift is attributed to a $\pi \rightarrow \pi^*$ antibonding transition and reflects a decrease within the material's optical energy gap energy. A narrowed band gap enhances the photocatalytic activity of the nanoparticles by enabling more effective the uptake of light in the visible region and improving this separation in the generation of charge carriers**.** The observed shift in absorption peaks confirms that Mn doping alters the arrangement of electronic states in Fe_2O_3 nanoparticles. These extent of this red shift was found to depend on the Mn doping concentration, suggesting a tuneable effect on the optical properties. These results demonstrate that Mn incorporation significantly alters the optical absorption behaviour, which in turn contributes to enhanced photocatalytic and magnetic functionalities of the synthesized nanomaterials.

The calculated band gap values for the samples indicate significant variation in their electronic properties, with Sample 1 at 3.535 eV, Sample 2 at 3.52 eV, Sample 3 at 3.43 eV, Sample 4 at 3.202 eV, and Sample 5 at 3.56 eV. Notably, Sample 5 exhibits the highest band gap, suggesting greater potential to generate electron-hole pairs under light irradiation. This higher band gap is beneficial for photocatalytic dye degradation, as it can facilitate more effective charge separation and reduce recombination, thereby enhancing the degradation efficiency. Conversely, the lower band gap of Sample 4 indicates increased light absorption in the visible region but may be associated with faster electron-hole recombination, slightly reducing its degradation performance. Overall, these band gap differences help explain the observed variations in dye degradation rates among the samples.

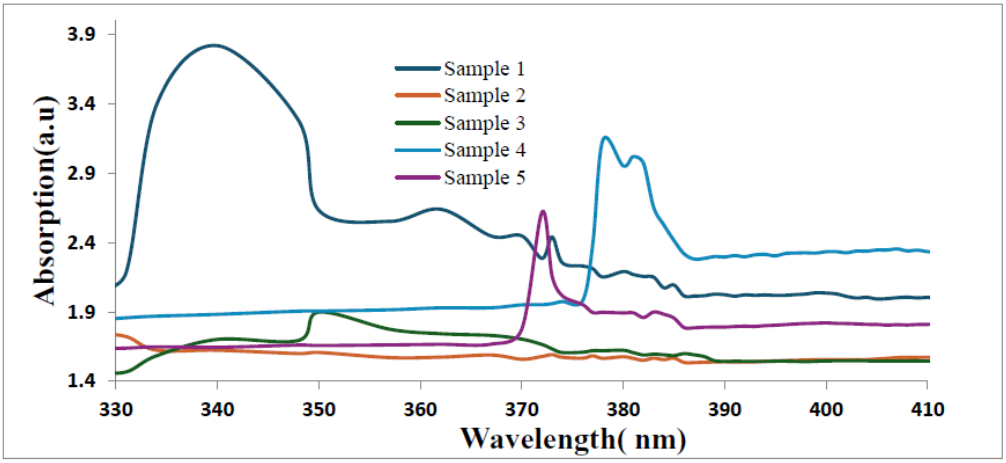

Fig. 6 – Combined UV-Vis spectrums.

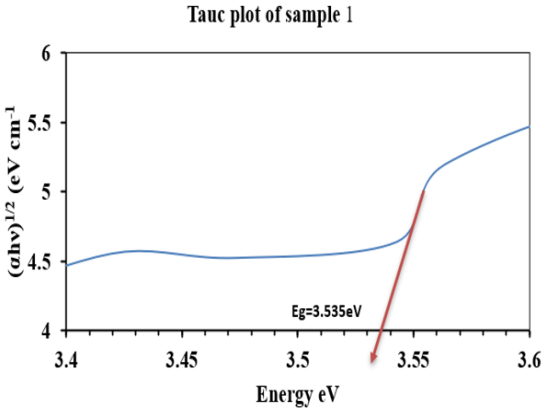

Fig. (a) Tauc Plot of Sample 1(Un-doped)

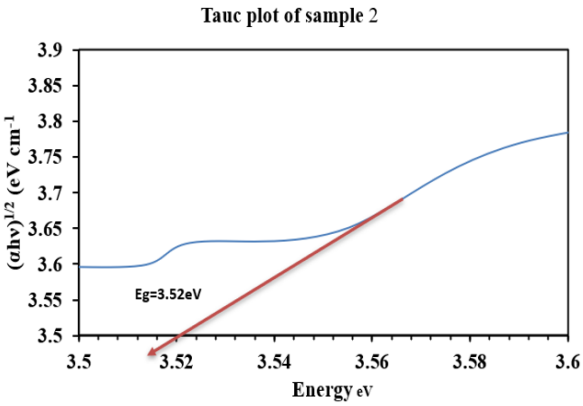

Fig. (b) Tauc Plot of Sample 2

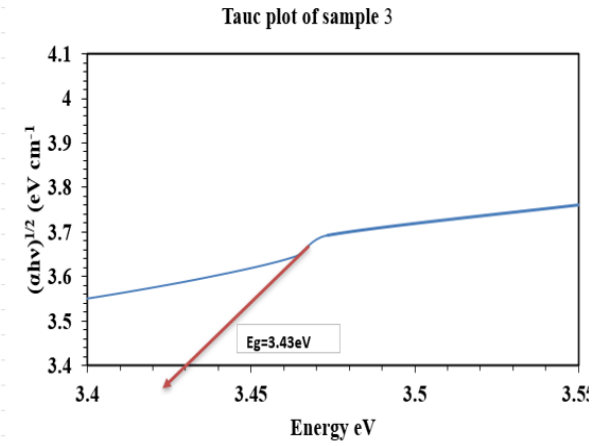

Fig(c). Tauc Plot of Sample 3

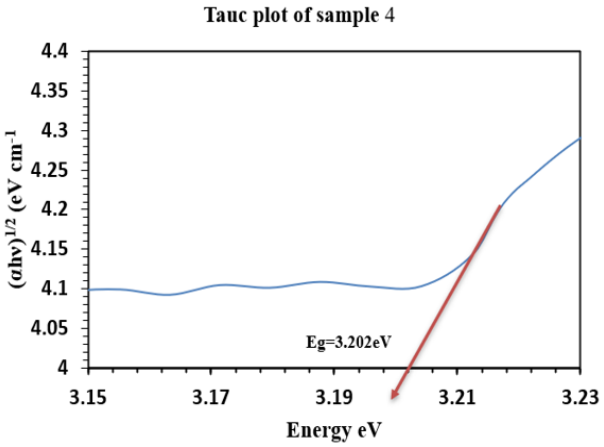

Fig (d).Tauc Plot of Sample 4

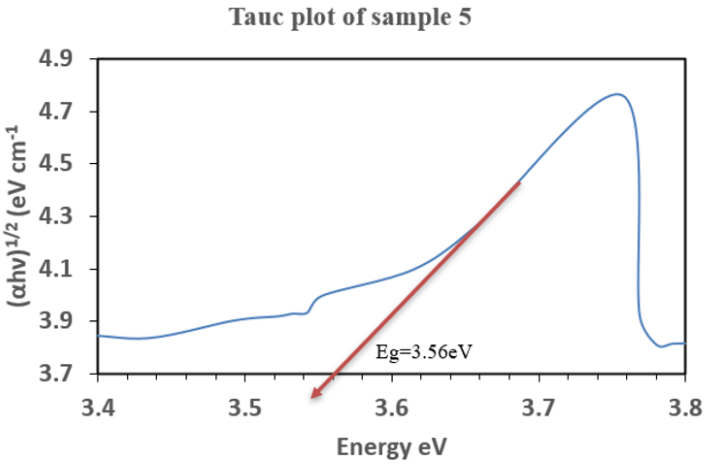

Fig (e). Tauc Plot of Sample 5

Fig. 7(a–e) – Tauc plot of iron oxide /Mn-doped iron oxide nanoparticles: a) Sample 1: undoped; b) Sample 2: 0.1 M; c) Sample 3: 0.2 M; d) Sample 4: 0.3 M, e) Sample 5: 1.5 M; f) combined graph.

Photocatalytic studies

The photocatalytic degradation of Indigo Carmine using Sample 5 (Mn–1.5 M) was systematically investigated under visible light irradiation. A solution was prepared by dissolving 0.01 g of Indigo Carmine in 100 mL of distilled water, and 0.001 g of Sample 5 was added as the photocatalyst. Prior to irradiation, the suspension was magnetically stirred in the dark for 30 min to achieve adsorption–desorption equilibrium. Photocatalytic experiments were conducted using a 300 W Xenon lamp as the visible light source, with an emission range of 400–700 nm and an intensity of approximately 100 mW/cm². The reaction temperature was maintained at 25 °C. Aliquots were withdrawn at 10 min intervals up to 70 min, centrifuged to remove the catalyst, and analyzed using UV-Vis spectroscopy to monitor the decrease in dye concentration. The wavelength versus absorbance spectra shows a gradual decrease in the characteristic absorption peak of Indigo Carmine with increasing irradiation time, indicating progressive dye degradation. The degradation profile demonstrates effective photocatalytic activity.

In the control experiment (without catalyst or without light), almost no change in absorbance was observed. This shows that the dye does not degrade on its own, and the degradation is mainly due to the photocatalyst.

For kinetic analysis, the degradation data was studied using a pseudo-first-order model:

$$\ln\left(\frac{A_0}{A}\right) = kt$$

The calculated rate constant (k) is 2.74 × 10^{-4} min^{-1}. The linear trend confirms that the reaction follows first-order kinetics.

The photocatalytic degradation of the dye at 610 nm was evaluated using seven replicates, with initial absorbances ranging from 0.390987 to 0.396766 (mean 0.3945 ± 0.0020). Measurements at 10-minute intervals revealed a gradual decrease in absorbance, indicating consistent degradation over time. Pseudo-first-order kinetic analysis gave a rate constant of 2.76×10^{-4} min^{-1}, which predicts that 75% degradation would occur in approximately 5024 minutes (~3.5 days) and 90% degradation in about 8347 minutes (~5.8 days). Although the reaction proceeds slowly, the data demonstrates reproducible photocatalytic activity and provides a clear quantitative understanding of the dye degradation process under the experimental conditions.

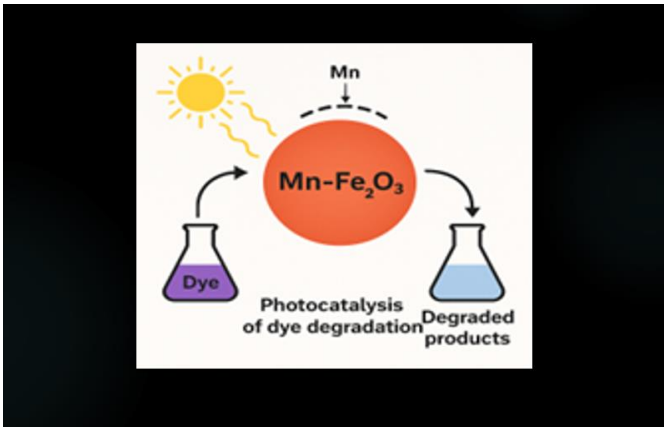

Fig. 8a – Photocatalytic degradation.

Calculating the degradation percentage with formula as follows:

Degradation (%) = $((C_0 - C_t)/C_0) \times 100 = ((A_0 - A_t)/A_0) \times 100$

where C_0 or A_0 = initial concentration or absorbance

C_t or At concentration or absorbance at time t

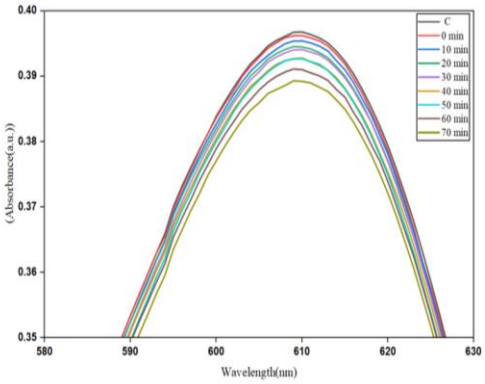

UV-Vis Spectra of Sample 5 at 10 min intervals during dye degradation

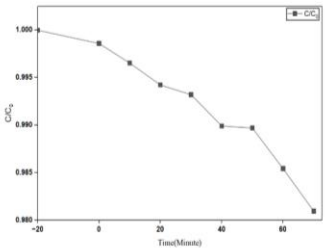

Degradation Kinetics (C/Co vs time) of Sample 5

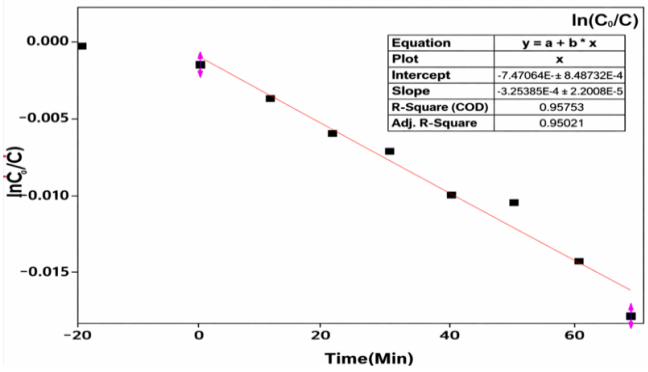

Pseudo- First order Kinetic plot(ln(C/Co) vs time) for dye degradation using Sample 5

Fig. 8b – Degradation analysis graph of Sample 5.

Mechanism of Photocatalytic degradation

When iron oxide is exposed to light, it absorbs the incoming energy and promotes electrons from the valence band into the conduction band, resulting in the formation of electron–hole pairs. The holes left behind in the valence band interact with water molecules, producing highly reactive hydroxyl radicals that initiate the oxidative breakdown of dye molecules. At the same time, the electrons transferred to the conduction band react with dissolved oxygen, generating superoxide radicals, which can further transform into additional hydroxyl radicals. Together, these reactive species progressively decompose the dye into harmless final products, primarily carbon dioxide and water.[33]

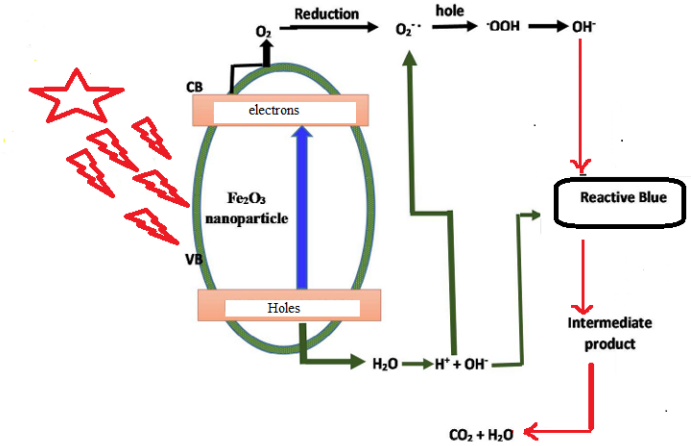

Fig. 9 – Pictorial representation of the degradation mechanism of by Iron Oxide NP.[33]

CONCLUSION

This study successfully synthesized manganese - doped iron oxide nano particles using co-precipitation method, aiming to enhance dye degradation efficiency. Characterization techniques confirmed the incorporation of Mn into the iron oxide lattice, resulting in the nanoparticles with modified structural and optical properties. The Mn doping led to a reduced band gap, facilitating improved photocatalytic activity under UV- visible irradiation. The doped nanoparticles demonstrated significant efficacy in degrading organic dyes, highlighting their potential application in water treatment. These finding suggests that Mn doped iron oxide nano particle are promising candidates for environmental remediation efforts.

REFERENCES

1. N. Fahimah, I.R.S. Salami, K. Oginawati, S.H. Susetyo, A. Tambun, A. N. Ardiwinata, S. Sukarjo, *J. Water l. Dev.*, **2023**, *56*, 153–163.
2. World Health Organization. Progress on sanitation and drinking water. 2015 Update and MDG Assessment.
3. J. Luo, S. Zhao, P. Wu, K. Zhang, C. Peng, S. W. Zheng, *J. Mater. Chem. C 3*, **2015,** 3391.
4. S.T. Shishiyanu, T.S. Shishiyanu, O.I. Lupan, *Sens. Actuators B*, **2005**, *107*, 379–386.
5. J. Lee, D. Lee, D. Lim, K. Yang, *Thin Solid Films*, **2007**, *515*, 6094–6098.
6. A.P. Periyasamy, *Sustainability*, **2024**, *16*, 495.
7. F.D. Chequer, G.A.R. de Oliveira, E.A. Ferraz, J.C. Cardoso, M.B. Zanoni, D.P. de Oliveira, *Eco-Friendly Textile Dyeing and Finishing*, **2013**, *6*, 151–176.
8. F. Lu, D. Astruc, *Coordination Chemistry Reviews*, **2020**, *408*, 213180.
9. A. G. Leonel, A. A. Mansur, H. S. Mansur, *Water research*, **2021**, *190*, 116693.
10. D. Enns, S. Cunze, N.J. Baker, J. Oehlmann, J. Jourdan, *Water Res*. **2023**, *243*, 120388.
11. S. Nizamuddin, M.T.H. Siddiqui, N.M. Mubarak, H.A. Baloch, E.C. Abdullah, S.A. Mazari, G.J. Griffin, M.P. Srinivasan, A. Tanksale, "Iron oxide nanomaterials for the removal of heavy metals and dyes from wastewater", Elsevier Inc., 2018. 10.1016/B978-0-12-813926-4.00023-9.
12. H. Liang, W. Chen, R. Wang, Z. Qi, J. Mi, Z. Wang, *Chem. Eng. J.*, **2015**, *274*, 224–230.
13. M.M. Berekaa, *Int. J. Curr. Microbiol. Appl. Sci.*, **2016,** *5*, 713–726. 10.20546/ ijcmas.2016.501.072.
14. M. Ismail, K. Akhtar, M.I. Khan, T. Kamal, M.A. Khan, A. M. Asiri, J. Seo, S.B. Khan, *Curr. Pharm. Des.*, **2019**, *25*, 3645–3663, https:// doi.org/10.2174/1381612825666191021142026.
15. S. Parveen, A.H. Wani, M.A. Shah, H.S. Devi, M.Y. Bhat, J.A. Koka, *Microb. Pathog*., **2018**, *115*, 287–292.
16. X. Qu, P.J.J. Alvarez, Q. Li, *Water Res*., **2013**, *47*, 3931 3946, https://doi.org/10.1016/j.watres.2012.09.058.
17. M. Sujana, S. Mohanty, *Int. J. Eng. Sci. Technol.*, **2011**, *2*, 1–12.
18. M. I. A. Abdel Maksoud, R. A. Fahim, A. G. Bedir, A. I. Osman, M. M. Abouelela, G. S. El Sayyad, D. W. Rooney, *Environmental Chemistry Letters*, **2022**, *20*, 1–44
19. J. Mathur, P. Goswami, A. Gupta, S. Srivastava, T. Minkina, S. Shan, D. Rajput, *Water*, **2022,** *14*, 3998.

20. I. Ali, V.K. Gupta, *Nat. Protoc*., **2006,** *1*, 2661–2667.
21. M. Anjum, R. Miandad, M. Waqas, F. Gehany, M. A. Barakat, *Arab. J. Chem*., **2019**, *12*, 4897–4919, https://doi.org/10.1016/j.arabjc.2016.10.004.
22. R. Mukhopadhyay, D. Bhaduri, B. Sarkar, R. Rusmin, D. Hou, R. Khanam, S. Sarkar, J. Kumar Biswas, M. Vithanage, A. Bhatnagar, Y.S. Ok, *J. Hazard. Mater.*, **2020**, *383*, https://doi.org/ 10.1016/j.jhazmat.2019. 121125 121125.
23. V.K. Chaturvedi, A. Kushwaha, S. Maurya, N. Tabassum, H. Chaurasia, M.P. Singh, Wastewater Treatment Through Nanotechnology: Role And Prospects, Restor. Wetl. Ecosyst. A Trajectory Towar. a Sustain. Environ., **2020**, 227–247. 10.1007/978-981-13-7665-8_14
24. R. Bhateria, R. Singh, *J. Water Process Eng*., **2019**, 31.
25. L. Ling, X.Y. Huang, W.X. Zhang, *Adv. Mater.*, **2018**, *30*, 1–6, https://doi.org/10.1002/ adma.201705703.
26. L. Machala, J. Tucek, R. Zboril, *Chem. Mater*., **2011**, *23*, 3255–3272.
27. P.C. Ricci, C.M. Carbonaro, R. Corpino, D. Chiriu, L. *AIP Conference Proceedings, American Institute of Physics***, 2015**, 104–110.
28. M. Al-Kuhaili, M. Saleem, S. Durrani, *J. Alloy. Compd.*, **2012,** *521*, 178–182.
29. V. Karade, S. Parit, V. Dawkar, R. Devan, R. Choudhary, V. Kedge, N. Pawar, J. Kim, A. Chougale, *Heliyon*, **2019**, *5*, e02044.
30. C.M. Hung, N.D. Hoa, N. Van Duy, N. Van Toan, D.T.T. Le, N. Van Hieu, *J. Sci.: Adv. Mater. Dev.*, **2016**, *1*, 45–50.
31. Y. Ge, M.I.U. Hoque, Q. Qu, *Electrochem. Energy Technol.*, **2019**, *5*, 1–6.
32. B. Show, N. Mukherjee, A. Mondal, *RSC Adv.*, **2016**, *6*, 75347–75358.
33. M. R. Hoffmann, S. T. Martin, W. Choi, D. W. Bahnemann, *Chemical Reviews*, **1995**, *95*, 69–96.